

Numerical Approach for Optically Limited Pulse Transmission in Polymer-Phthalocyanine Composite Systems

Seán M. O’Flaherty,^{*,†} James J. Doyle,[‡] and Werner J. Blau[‡]

European Synchrotron Radiation Facility, Grenoble, France, and Department of Physics,
Trinity College Dublin, Republic of Ireland

Received: July 7, 2004; In Final Form: September 4, 2004

The use of guest–host systems, where phthalocyanines assume the role of guest inclusions in an otherwise homogeneous host polymer film, is a feasible method toward applying the phthalocyanine moiety in a solid-state passive optical limiter. In this contribution, a preparation method for the fabrication of such composite films followed by optical limiting experiments in the nanosecond regime at 532 nm is presented for Zn phthalocyanines. A simple approximate nonlinear absorption coefficient based on molecular orbital analysis is developed allowing one use of two “yardstick” parameters to quantify the nonlinear optical response. Additionally this nonlinear absorption coefficient is folded with the distribution of energy in the exciting pulse to model more closely the experiment and it is shown that by omission of this spatial resolution one may underestimate the numerical magnitudes of the nonlinear optical parameters.

1. Introduction

The use of lasers as the driving force of information processing for future photonic technologies is almost inevitable. As a direct consequence of this, the protecting of targets from high-intensity strayed or targeted optical beams, the most important being the eye, via optical limiting (high suppression of high-intensity optical beams while allowing high transmission of ambient light) is a task of immediate importance. The field of optical limiting has invested much effort into the research of materials and processes in an attempt to afford some measure of protection for such circumstances. Consequently, phthalocyanines (Pc) and their derivatives have emerged as promising materials for consideration owing to their large optical nonlinearities, ultrafast response times, high versatility, and easy processability.¹

Processes that might be useful for passive optical limiting inevitably involve some form of nonlinear response to light. Among these are nonlinear absorption, nonlinear refraction, and nonlinear scattering. Phthalocyanines are materials that optically limit by population of excited states through multistep nonlinear absorption, leading to reverse saturable absorption (RSA), under visible (~400–600 nm) irradiation. It has been shown that phthalocyanine (Pc) compounds exhibit RSA because of a relatively efficient intersystem crossing, usually spin-forbidden, but for phthalocyanines facilitated by spin–orbit coupling from the lowest excited singlet state (S_1) to the lowest triplet state (T_1), and the subsequent increase in the population of the T_1 state during the laser pulse.

There have been many studies reported of optical limiting by solutions of phthalocyanines chemically modified in diverse manners since the first report for the chloroaluminum phthalocyanine (PcAlCl).² Consequently, solution nonlinear-spectroscopy has dominated research in the optical limiting field with

phthalocyanines in recent times, owing mainly to investigations of the many dramatic and profound new phthalocyanines that have been synthesized.^{3–16} Fewer studies have considered the practical application of such compounds which would almost inevitably involve the solid-state casting of such compounds in some manner.^{17–21} The use of guest–host systems, where phthalocyanines assume the role of guest inclusions in an otherwise homogeneous host polymer film is a feasible method toward applying the phthalocyanine moiety “en route” for real-world optical limiting applications. In this contribution we will discuss such composite films as passive solid-state optical limiters. The sample preparation method and optical quality of the produced limiters will be discussed. A simple approximate nonlinear absorption coefficient based on molecular orbital analysis will be derived allowing one use of two “yardstick” parameters to quantify the response in ns optical limiting experiments. This nonlinear absorption coefficient will be folded within a numerical algorithm that considers the distribution of energy in the exciting pulse. It will be shown that by not considering this spatial resolution that one will significantly underestimate the nonlinear optical parameters within a sample medium.

2. Background and Numerical Methods

Nonlinear Absorption Coefficient. To discuss the importance of the various parameters that influence RSA in the phthalocyanine system, a general five-level model such as that shown in Figure 1 has been considered, and approximations suitable for the phthalocyanine system under nanosecond irradiation have been applied. The vibrational levels of the electronic states are ignored and for the sake of simplicity the laser pulse width is assumed to be longer than any of the lifetimes associated with the levels. To further simplify matters, it was assumed that relaxation out of states S_2 and T_2 is very rapid so that the population of these two levels may be neglected.

Generally for this five-level system after initial excitation, the first excited singlet state S_1 is populated, from here the electrons may be subsequently excited into S_2 within the pulse

* To whom correspondence should be addressed. E-mail: sean.oflaherty@physics.org.

[†] European Synchrotron Radiation Facility.

[‡] Trinity College Dublin.

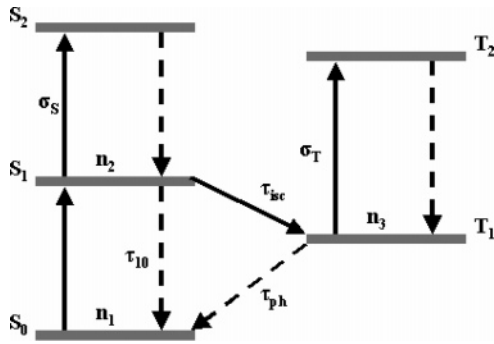


Figure 1. Generalized five-level system used in deriving the excited-state absorption model used to simulate RSA in the phthalocyanine system. S_i represents singlet levels, and T_i represents triplet levels. Solid arrows imply an excitation resulting from photon absorption and dashed arrows represent relaxations.

width of the laser. Once in S_2 , they rapidly relax to S_1 again. From S_1 , the population may undergo an intersystem crossing to the first excited triplet T_1 with a time constant τ_{isc} and thereafter undergo excitations and relaxations to and from T_2 . Thus, the population is exchanged cyclically between S_1 and T_1 , as the lifetime of T_1 (τ_{ph}) is very long in comparison to τ_{isc} . Furthermore, stimulated emission from S_1 is excluded due to the small fluorescence quantum yield. The system now reduces to the following set of three differential rate equations

$$\frac{\partial n_1}{\partial t} = -\frac{\sigma_0 I}{h\nu} n_1 + \frac{n_2}{\tau_{10}} + \frac{n_3}{\tau_{ph}} \quad (1)$$

$$\frac{\partial n_2}{\partial t} = \frac{\sigma_0 I}{h\nu} n_1 - \frac{n_2}{\tau_{isc}} - \frac{n_2}{\tau_{10}} \quad (2)$$

$$\frac{\partial n_3}{\partial t} = \frac{n_2}{\tau_{isc}} - \frac{n_3}{\tau_{ph}} \quad (3)$$

where n_1 , n_2 , and n_3 refer to the populations of S_0 , S_1 , and T_1 . Attenuation of the laser beam is governed by a propagation equation where the absorption coefficient now includes the excited-state absorption from S_1 and T_1

$$\frac{\partial I}{\partial z} = -\alpha I = -(\sigma_0 n_1 + \sigma_s n_2 + \sigma_T n_3) I \quad (4)$$

Under the steady state approximation, which is valid when the pulse width is much longer than any relaxation time, all of the time derivatives may be set to zero. This is a valid assumption for nanosecond pulses as the lifetimes in phthalocyanines are typically of order picoseconds, for example tetrasubstituted indium phthalocyanines.¹⁰ In this case, the equation can be easily solved analytically, and the intensity dependent absorption coefficient becomes¹⁴

$$\alpha(I, I_{sat}, \kappa) = \frac{\alpha_0}{1 + \frac{I}{I_{sat}}} \left(1 + \kappa \frac{I}{I_{sat}} \right) \quad (5)$$

by defining $\kappa = \sigma_{ex}/\sigma_0$, and noting that σ_{ex} and σ_0 are the absorption cross-sections of the ground and the excited transitions respectively, and $I_{sat} = h\nu/(\sigma_0 \tau_{10})$.²² Thus, this effectively reduces the five-level model to a three-level model. This model, though simple, reproduces the gross effects of RSA and highlights the crucial role that the excited-state absorption plays in the overall absorption coefficient. Within this expression for

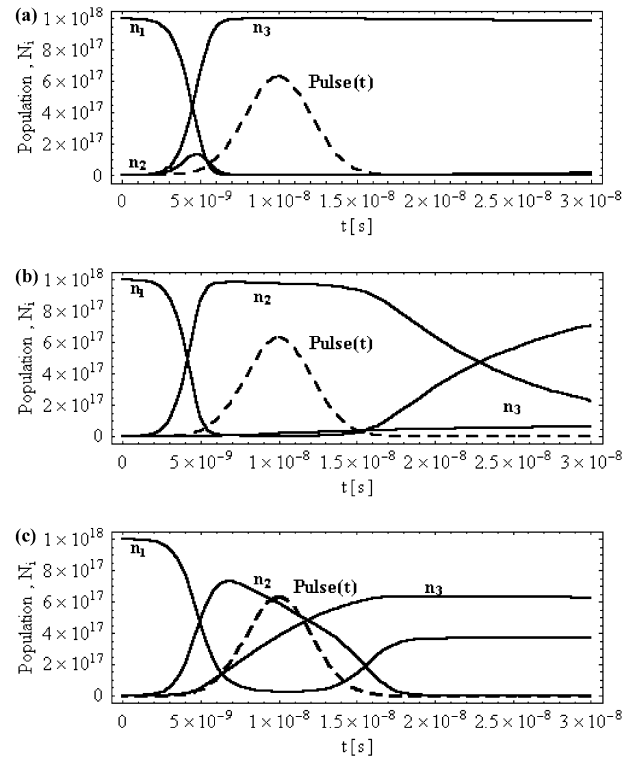


Figure 2. Temporal evolution of the ground, first excited singlet and first excited triplet states of the populations for (a) simulation 1, (b) simulation 2, and (c) simulation 3. The dashed Gaussian curve represents temporal profile of the incident incident laser pulse, which has been set to peak at 10 ns after the start of the simulation.

TABLE 1: Numerical Values Used in the Simulations for the Phthalocyanine System

parameter	simulation 1	simulation 2	simulation 3
τ_{fwhm} [ns]	6	6	6
λ [nm]	532	532	532
N	1×10^{18}	1×10^{18}	1×10^{18}
N	1×10^{18}	1×10^{18}	1×10^{18}
I_0 [GW cm ⁻²]	0.1	0.1	0.1
σ_0 [cm ⁻²]	1.8×10^{-18}	1×10^{-18}	1×10^{-18}
τ_{10} [ns]	0.5	5	0.5
τ_{isc} [ns]	0.3	300	10
τ_{ph} [μ s]	1	1	1

the nonlinear absorption coefficient, one can then state that higher κ values combined with lower F_{sat} values define more efficient optical limiters. This steady state model approximates to a dynamic model in the limit of temporally long pulse widths, i.e., nanosecond irradiation when all other lifetimes in the material are of the order of picoseconds.

In the proceeding paragraphs, numerical simulations of the population dynamics of the rate equations presented in eqs 1–3 will be presented to investigate the nature of the nonlinear absorption coefficient expressed in eq 5. Initially the populations at $t = 0$ s were set as $n_1(0) = N$, and $n_2(0) = n_3(0) = 0$. The pumping pulse that was used was of temporally Gaussian profile with $\tau_{fwhm} = 6$ ns and $\lambda = 532$ nm to match the laser that will be used in the experiments. The pulse peak was set to occur 10 ns after the start of the simulation in all cases.

In the first simulation (Figure 2a), the population dynamical behavior for the chloroindium phthalocyanine studied by Shirk et al.,¹⁰ Perry et al.,¹⁷ and Chen et al.⁸ has been modeled. Shirk et al.¹⁰ reported that the intersystem crossing in this system was of 0.3 ns and Perry et al.¹⁷ reported that the ground-state absorption cross-section was of the order of 1.8×10^{-18} cm²,

whereas Chen et al.⁸ have reported that the fluorescence lifetime is of the order of 0.5 ns for this compound. It can be seen in Figure 2a that the population in S_1 represented by n_2 peaks just before 5 ns. From this point on, the short intersystem crossing time facilitates the rapid transfer of the population into the T_1 level, measured by n_3 . The n_1 population in S_0 is rapidly depleted tending toward zero after about 6 ns. Comparison with the laser pulse profile (dashed line) shows that the pulse is still relatively weak at this time, and therefore, for the majority of the event, the population in T_1 undergoes excitations and subsequent rapid relaxations to and from higher triplet states. This is in excellent agreement with the assumptions made when deriving the static case nonlinear absorption coefficient above and implies that in this regime with the short intersystem crossing time the nonlinear absorption coefficient described by eq 5 is thus spectroscopically accurate, where σ_{ex} defines triplet absorption.

The opposite situation to the entire transfer of population to the T_1 level is where the intersystem crossing relative to the pulse is extremely long (300 ns in Figure 2b). In this case, it can be seen that the population in T_1 , denoted n_3 , grows only slightly and slowly and that the vast majority of the population resides in S_1 undergoing higher singlet excitations and subsequent vibrational relaxations back to S_1 during the pulse. In this regime, the nonlinear absorption coefficient described by eq 5 is again spectroscopically accurate where the nonlinear absorption cross-section σ_{ex} is due almost entirely to singlet state transitions.

Each of the previous cases exhibits high-intensity optical excitations in either the triplet levels or the singlet levels exclusively, which can be described by an effective three level absorption coefficient. Intersystem crossing with a lifetime of the order of the pulse width describes the transitional regime between these two extremes. This has been modeled in the third simulation (Figure 2c) where the intersystem crossing, τ_{isc} , has been set to 10 ns which is comparable to the 6 ns laser pulse. It can be seen in the figure that during the high-intensity region of the laser pulse centered about 10 ns after the commencement of the simulation that the S_1 and T_1 populations, n_2 and n_3 , respectively, are both of similar magnitude. Consequently, the energy dissipation of the laser pulse involves both the singlet and triplet manifolds. If this system is treated with a simplified three-level model, the nonlinear absorption cross-section results from a combination of both the singlet and triplet absorptions. In this case, the model is not spectroscopically accurate but can be used to calculate effective excited to ground-state absorption cross-section ratios that can be used to describe the magnitude of the nonlinear absorption regardless of the source of the dissipation. The three-state model is used in all cases to fit the nonlinear absorption in this work and it is recognized that in general the model may not be spectroscopically exact. The intention of this model is therefore to attempt to link the magnitude of the nonlinear response with the mathematical parameters κ and F_{sat} .

Before application of the nonlinear absorption coefficient to experimental data, $\alpha(I, I_{\text{sat}}, \kappa)$ has to be substituted back into the propagation formalism. One can then consider an integral over a homogeneous sample of thickness L where the integration is performed with limits on dz going from $z = 0 \rightarrow L$ and the limits on dI going from $I = I_{\text{in}} \rightarrow I_{\text{T}}$

$$\int_{I_{\text{in}}}^{I_{\text{T}}} \left(\frac{1}{1 + I/I_{\text{sat}}} + \frac{\kappa I/I_{\text{sat}}}{1 + I/I_{\text{sat}}} \right)^{-1} \frac{dI}{I} = -\alpha_0 \int_0^L dz \quad (6)$$

This expression can then be sequentially integrated and by

defining the transmission T as $T = I_{\text{T}}/I_{\text{in}}$ a transcendental equation for T , where T is essentially a function of I , κ and I_{sat} can be readily derived

$$T(I, \kappa, I_{\text{sat}}) = \exp(-\alpha_0 L) \left(\frac{I_{\text{sat}} + \kappa T(I, \kappa, I_{\text{sat}}) I}{I_{\text{sat}} + \kappa I} \right)^{1-1/\kappa} \quad (7)$$

It can be noted that the intensity (I) and the pulse energy density defined as $F = E_{\text{tot}}/(\pi w(z)^2)$, where E_{tot} is the energy per pulse and $\pi w(z)^2$ is the surface area through which the portion of the pulse is propagating at any position denoted by z , are directly related to each other and consequently the parameter I/I_{sat} can be replaced with F/F_{sat} in eq 5, where in this case F_{sat} is the energy density saturation.

Numerical Resolution of the Spatial Energy Profile

If an optical pulse is considered to be propagating in the z direction in space, then it will possess a certain spatial distribution of its energy in the x - y plane perpendicular to its' propagation. Frequently, and indeed for the optical pulses that will be utilized anon in the Experimental Section, this energy profile is symmetric in the x and y directions and Gaussian in its radial distribution. If one defines w as the half-width at e^{-1} times the maximum intensity within the distribution, then the normalized double integral of this Gaussian governed bell-shape in three-dimensional space can be mathematically expressed as follows:

$$\frac{1}{\omega^2 \pi} \int_{y=-\infty}^{y=+\infty} \int_{x=-\infty}^{x=+\infty} \exp \left\{ -\frac{x^2 + y^2}{w^2} \right\} dx dy = \frac{1}{\omega^2 \pi} \int_{\theta=0}^{\theta=2\pi} \int_{r=0}^{r=+\infty} r \exp \left\{ -\frac{r^2}{w^2} \right\} dr d\theta = 1 \quad (8)$$

The term found on the most left of the LHS is the integral defined in Cartesian coordinates (x, y, z), whereas the second central term is the symmetrically more convenient formulation in cylindrical coordinates (r, θ, z) where $r^2 = x^2 + y^2$ and where θ defines angular displacements about the z axis. One can then consider the entire energy in the pulse at any instant E_{tot} being composed of energy contributions $E(r, \delta r, \delta \theta)$ contained within the discrete spatial regions defined by θ to $\theta + \delta \theta$ and r to $r + \delta r$ in the (r, θ) plane

$$E(r, \delta r, \delta \theta) = \frac{E_{\text{tot}}}{w^2 \pi} \int_{\theta=\theta}^{\theta=\theta+\delta\theta} d\theta \int_{r=r}^{r=r+\delta r} r \exp \left\{ -\frac{r^2}{w^2} \right\} dr \quad (9)$$

Additionally, symmetry implies that θ is somewhat redundant because for any given r the energy is equal for all θ , and exploiting such symmetry, the double integral can be reduced to a single integral over r . Therefore, one can consider the energy increments contained within the annular sections defined by the radial values contained within r and $r + \delta r$. The average energy density $F(r, \delta r)$ (average energy per unit area) in each section can then be defined as the integrated energy within that section divided by its two-dimensional area in the (r, θ) plane $A(r, \delta r)$ and can be expressed mathematically as

$$F(r, \delta r) = \frac{E(r, \delta r)}{A(r, \delta r)} = \frac{2}{((r + \delta r)^2 - r^2)} \frac{E_{\text{tot}}}{w^2} \int_{r=r}^{r=r+\delta r} r \exp \left\{ -\frac{r^2}{w^2} \right\} dr \quad (10)$$

This can be easily approximated in a numerical algorithm where r spans from $r = r_0 = 0$ to its maximum value $r = r_n$ (theoretically ∞) in n steps where the energy density of the i th region $F(r_i, r_{i+1})$ is defined as

$$F(r_i, r_{i+1}) = \frac{2}{(r_{i+1}^2 - r_i^2)} \frac{E_{\text{tot}}}{w^2} \int_{r=r_i}^{r=r_{i+1}} r \exp\left\{-\frac{r^2}{w^2}\right\} dr \quad (11)$$

Similarly, the entire energy E_{tot} can be formulated as the sum over the energy contained within each of the separate n annular regions

$$E_{\text{tot}} = \sum_{i=0}^{n-1} E(r_i, r_{i+1}) = \sum_{i=0}^{n-1} \left\{ 2\pi \frac{E_{\text{tot}}}{w^2} \int_{r=r_i}^{r=r_{i+1}} r \exp\left\{-\frac{r^2}{w^2}\right\} dr \right\} \quad (12)$$

In application, the choice of n (and accordingly δr) and r_n can be chosen such that the preceding equation remains valid within numerical precision. For example, if an insufficient maximum radius r_n or number of steps n are chosen, the sum over the energies of the annular sections will be different than that of the starting value E_{tot} .

At this juncture, it becomes clear that for any given pair of nonlinear optical coefficients κ and F_{sat} , assuming that the waist size of the beam w and the pulse energy E_{tot} are known, one can consider first a spatial decomposition of the incident pulse following the method just detailed above, followed by independent analysis within the sample medium of each decomposed annular section. Each energy density $F(r_i, r_{i+1})$ contained within the annular section defined by r_i and r_{i+1} can be separately propagated through the sample medium, the interaction being modeled by the transcendental equation quoted above (eq 7). Therefore for each $F(r_i, r_{i+1})$ the transmission coefficient can be found numerically. These transmission coefficients can then be recombined with their respective incident components to create the spatial profile of the transmitted pulse defined by its own energy and the nonlinear optical response of the sample medium.

The spatial decomposition of a Gaussian pulse, with physical parameters typical of that which will be used subsequently for experiments, followed by a propagation of each decomposed subdivision of the pulse through a sample medium and recombination after the light-medium interaction will be presented here. For the purposes of producing an appreciable nonlinear response the materials' physical properties were defined so that $\alpha_0 L = 0.1$, $\kappa = 20$, and $F_{\text{sat}} = 5 \text{ J cm}^{-2}$. The waist radius was set so that $w = 20 \mu\text{m}$ and the pulse was given total energy $E_{\text{tot}} = 100 \mu\text{J}$. In Figure 3a, the plot depicts the energy density (J cm^{-2}) of the input and transmitted pulses as a function of the spatial radial position from the intensity maximum on the z axis. For the calculation presented here, the pulse was arbitrarily decomposed and subsequently integrated from $r = 0$ to $r = 3.75w$ using 150 equally spaced annular sections. It was found that the entire normalized integral over the pulse did not differ from the sum over the 150 decomposed integrals within floating point numerical precision. In the inset to this figure, a three-dimensional rendering of the incident and transmitted pulses are presented where the input pulse (on the left) is shifted from the z axis by $(-60, -60) \mu\text{m}$ in the x - y plane and the transmitted pulse (to the right) is shifted in the same plane by $(60, 60) \mu\text{m}$ for clarity. The difference in spatial profile of the energy distribution of the input and output pulses

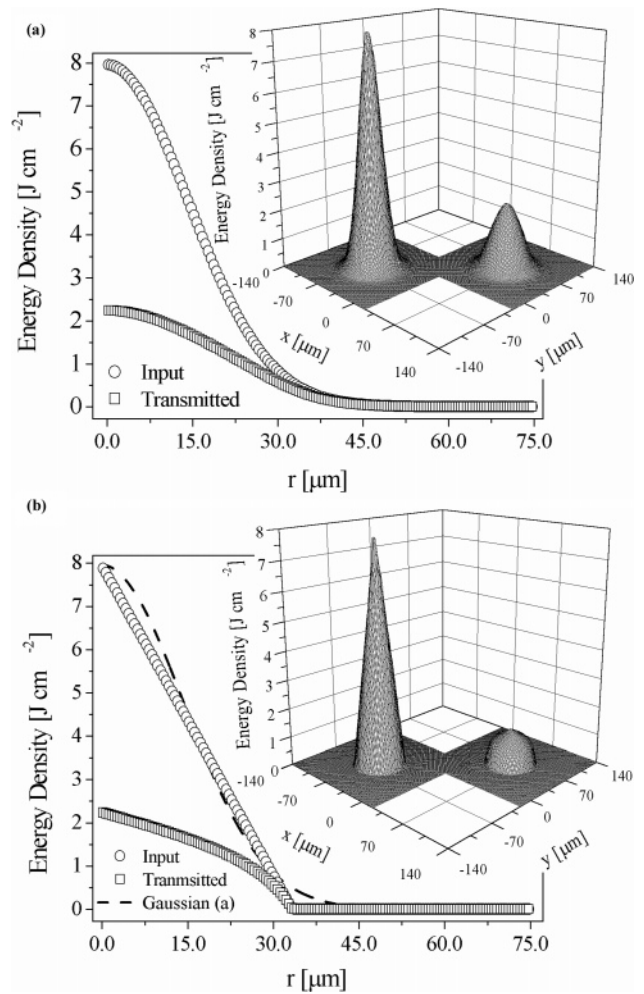


Figure 3. (a) Simulation of spatial decomposition of a Gaussian pulse followed propagation of each subdivision through a sample medium with $\alpha_0 L = 0.1$, $\kappa = 20$, $F_{\text{sat}} = 5 \text{ J cm}^{-2}$, $w = 20 \mu\text{m}$, and total pulse energy $E_{\text{tot}} = 100 \mu\text{J}$. Pulse was decomposed and integrated from $r = 0$ to $3.75w$ using 150 equally spaced annular sections. A three-dimensional rendering of the incident and transmitted pulses are presented in the inset. (b) Similar simulation with a hypothetical conical pulse, where the dashed line represents the profile of the Gaussian pulse used in (a).

can be easily seen where the output pulse is essentially also Gaussian in shape simply with lower energy densities in the higher energy section of the pulse.

One of the significant benefits of the method of splitting the pulse is that in principle any pulse shape can be considered. As an example to demonstrate this generality, an unrealistic hypothetical conical pulse is presented in Figure 3b. In the figure, the two-dimensional shape of the Gaussian pulse discussed in the preceding paragraph is included to allow a direct comparison of the two input pulse shapes. As before in the inset to this figure, a three-dimensional rendering of the incident and transmitted pulses is shifted for clarity as in Figure 3a. After interaction within the medium, it can be seen that the spatial distribution of the output pulse is no longer conical, where it has assumed a much more complicated distribution of its energy. In general, this method can be applied to any spatial distribution of energy although computation time for distributions asymmetric about the z axis would be significantly increased, as the double integral (eq 9) in such an asymmetric geometry could not be reduced to integration in a single dimension.

In an optical limiting experiment, one generally monitors the energy of the incident pulses in tandem with the waist diameter

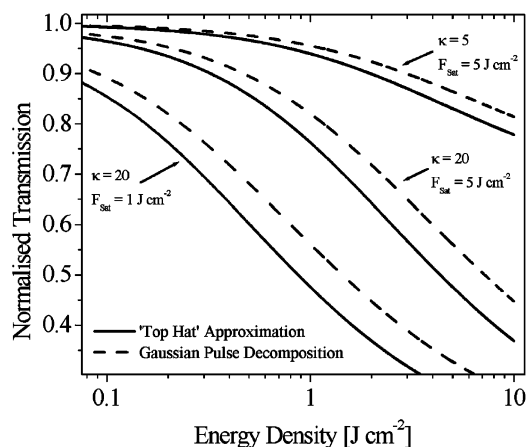


Figure 4. Typical optical limiting plots of transmission as a function of energy density simulated using eq 7 with the two distinctly different methods, solid lines represent a “top hat” approximation where the spatial distribution of the pulses energy is ignored and for the dashed lines the Gaussian profile of the pulse is considered using the theory detailed in section 2.

of the beam, and it has become somewhat commonplace to illustrate the data as output intensity, energy density (J cm^{-2}), or transmission percentage against the incident parameter. Generally, the spatial component involved in the calculation of either the energy density or the intensity is governed by the active area of the beam and normally defined by πw^2 , where w is the waist radius at e^{-1} times the intensity as defined above. In this contribution, experimental data will be presented as transmission as a function of this “somehow” averaged incident energy density ($F = E_{\text{tot}}/\pi w^2$). In the remaining paragraphs, it will be demonstrated however that if one adopts a similar approach with the theoretical analysis, i.e., an essentially “top hat” squared pulse of circular base (x – y plane) is assumed in fitting eq 7 to the data and the Gaussian spatial profile of the pulse is ignored, then one will significantly underestimate the optical coefficients, (κ and F_{sat}).

In Figure 4, optical limiting plots of transmission as a function of energy density are simulated using eq 7 with the two distinctly different methods, where in one case the “top hat” approximation is used (solid lines) and in the other the Gaussian profile of the pulse is considered using the theory detailed throughout this section (dashed line). It can be seen in the figure that if one considers the strength of the nonlinear attenuation the “top hat” approximated pulse outperforms the Gaussian decomposed simulation for all values of F with equal κ and F_{sat} magnitudes. Consequently, to achieve similar curves, higher magnitudes of κ and lower F_{sat} have to be inserted into the algorithm that considers the spatial resolution of the pulses energy. Thus, if one were to fit this curve (“top hat” approximation) to a dataset then the numerical values of the yielded nonlinear coefficients (κ , F_{sat}) would be in fact different than those produced considering the Gaussian spatial profile of the pulse, and given that high κ and low F_{sat} are desirable one would certainly underestimate the optical limiting efficiency of the system.

A computer code has been developed that fits a theoretical curve to transmission as a function of incident energy density data. For each energy density–transmission (F , T) observation in the dataset, the spatial profile of a pulse with this “averaged” F is created and decomposed into incremental annular sections, then each section is propagated through the sample medium and the transmitted pulse annular sections are recombined afterward. The light–matter interaction of each annular section in the medium is governed by the transcendental equation (eq

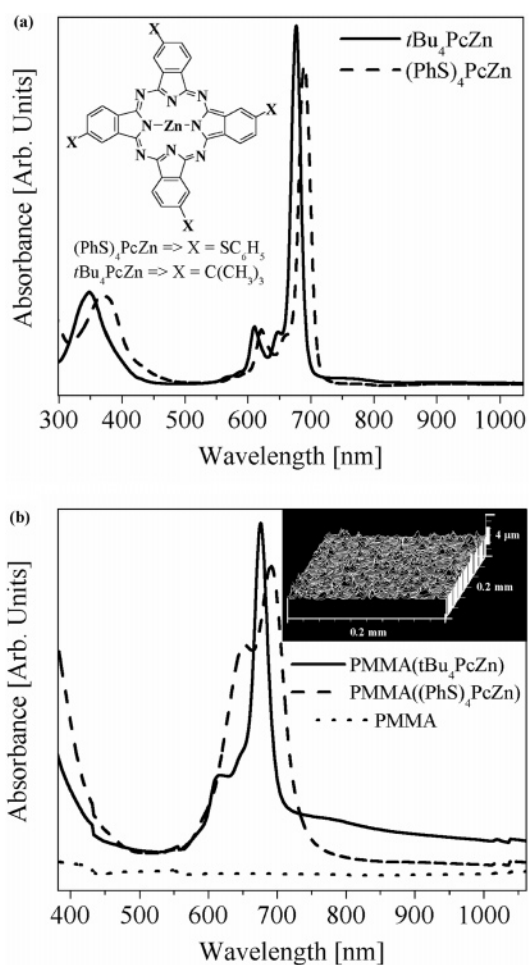


Figure 5. Linear UV–vis absorption spectra for solutions (a) of $t\text{Bu}_4\text{PcZn}$ and $(\text{PhS})_4\text{PcZn}$ at 0.5 g L^{-1} in spectroscopic grade toluene and (b) of $\text{PMMA}(t\text{Bu}_4\text{PcZn})$, $\text{PMMA}((\text{PhS})_4\text{PcZn})$, and PMMA films. The phthalocyanine structures are sketched in the inset to (a) and a three-dimensional rendering of the surface ($0.2 \text{ mm} \times 0.2 \text{ mm} \times 4 \mu\text{m}$) of the $\text{PMMA}(t\text{Bu}_4\text{PcZn})$ film determined using interferometry is depicted as an inset to (b).

7) which requires a numerical solution with $T(F, \kappa, F_{\text{sat}})$ treated as the dependent variable, F is the independent variable, and this entire process is enclosed within an outer envelope algorithm where κ (realistically σ_{ex} as α_0 was measured) and F_{sat} are both free parameters.

3. Experimental Section

The samples investigated in this study were solution studies of two different dissolved zinc phthalocyanines and composite films fabricated by embedding these phthalocyanine compounds in a host polymer. The phthalocyanines exploited were $(\text{PhS})_4\text{PcZn}$ (Aldrich, Product Code: 418234) and $t\text{Bu}_4\text{PcZn}$ (Aldrich, Product Code: 430994), (see inset to Figure 5a for chemical structure sketches). The host polymer chosen was poly(methyl-methacrylate), PMMA. Initially the polymer was dissolved in the solvent cyclohexanone at a concentration of 100 g L^{-1} . This required approximately 40 h of low power (60 W) agitation in a sonic bath to form a clear viscous solution. The phthalocyanines were added to this solution at a mass ratio of 1:5 (Pc:PMMA), thus implying a 10 g L^{-1} partial concentration of the phthalocyanine in the solution. Multilayer films were then cast using a conventional spin coating system where the quartz substrate was spun at 1000 rpm without ramping. The film was baked at 55°C for 90 min between successive layers

where it was seen to grow in thickness by a few μm for each layer, and the finished optically homogeneous films had a deep glassy blue or green appearance for the PMMA(*t*Bu₄PcZn) and PMMA((PhS)₄PcZn) films, respectively. Solutions of both phthalocyanines at 0.5 g L⁻¹ in spectroscopic grade toluene were also prepared for comparison reasons.

The linear optical properties of the materials used in this study were measured using a Shimadzu UV3100 UV-vis-NIR spectrometer. In conjunction with the linear optical investigation, the morphology of the film surface—air interface was investigated using a Zygo white light interferometer. This technique allows for detailed three-dimensional surface rendering by probing the interference pattern created along a selected surface area. Film thickness measurements were made using the same technique. All optical limiting experiments described in this study were performed using ≈ 6 ns Gaussian pulses from a Q switched Nd:YAG laser. The beam was spatially filtered to remove the higher order modes and operated at its second harmonic, 532 nm, with a pulse repetition rate of 10 Hz.

4. Results

The linear UV-vis absorption spectra for the solutions and films are presented in Figure 5. In Figure 5a, solutions of *t*Bu₄PcZn and (PhS)₄PcZn at 0.5 g L⁻¹ in spectroscopic grade toluene are presented, and in Figure 5b, the spectra of the PMMA(*t*Bu₄PcZn) and PMMA((PhS)₄PcZn) composite films are presented. In Figure 5b, a spectrum of a pure PMMA film without any other inclusions has been added and it can be seen that the PMMA has a flat profile of low absorbance over the visible region as evidenced by its clear appearance. The Q-band for both films containing phthalocyanines is broadened for the films compared to the solutions indicative of aggregated behavior, not unexpected owing to the large partial concentration of 20 g L⁻¹ that was used in the film construction and the fact that the solid state is naturally more condensed. The spectral position of the Q-band is not significantly shifted for the solution to solid state transition (only by about 2 nm to red for the (PhS)-4PcZn case and by about 1 nm to the blue for the *t*Bu₄PcZn case). It can be seen that the “window region” between the Q- and B-bands is preserved, although slightly narrowed, in the films indicating that the films are also suitable for optical limiting of 532 nm light. It is significant that PMMA required something in the region of 40 h of low power sonic agitation to completely dissolve in cyclohexanone as it is exactly this that facilitates the “growing” of the film thickness through repeated spin casting. The films in this study generally required 10–15 layers to reach the required thicknesses. Visibly, one could see through the film without distortion of the transmitted images verifying qualitatively its optical homogeneity. The interfacial film—air roughnesses (σ_i) of the composite films determined from the interferometry studies revealed that the film—air interface was relatively smooth in relation to the wavelength (532 nm) used later to probe the nonlinear optical properties. A sample three-dimensional rendering (0.2 mm \times 0.2 mm \times 4 μm) for the rougher PMMA(*t*Bu₄PcZn) film is included as an inset to Figure 5b. For the PMMA((PhS)₄PcZn) and PMMA(*t*Bu₄PcZn) composites, one can note the roughness magnitudes of approximately 21 and 110 nm respectively. Thus, embedding phthalocyanines in PMMA for fabrication of multilayer optical limiting films, in this case up to 15 successive layers, has been shown to be useful technique to produce a high quality film.

The optical limiting response of all four systems investigated in this study is presented in Figure 6. The solid lines are theory

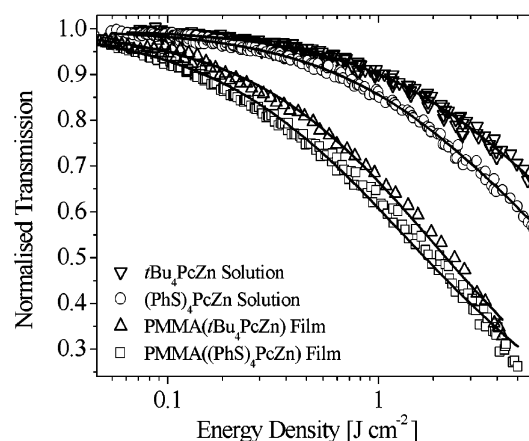


Figure 6. Optical limiting plots for all systems investigated in this study, where the response is represented as normalized transmission as a function of incident energy density. The solid lines are theory fits to the data using the expressions detailed in section 2 where the spatial distribution of the energy in the pulse has been considered.

TABLE 2: Optical Coefficients for the Materials Measured in This Study^a

material	σ_i [nm]	L [μm]	α_0 [cm ⁻¹]	k [$\sigma_{\text{ex}}/\sigma_0$]	F_{sat} [J cm ⁻²]
<i>t</i> Bu ₄ PcZn (S, 0.5 g L ⁻¹)		1000	1.64	11.2 \pm 0.6	8.8 \pm 0.6
(PhS) ₄ PcZn (S, 0.5 g L ⁻¹)		1000	1.49	13.0 \pm 0.4	5.7 \pm 0.2
PMMA(<i>t</i> Bu ₄ PcZn) (F)	110	34.5	207.1	6.7 \pm 0.2	3.6 \pm 0.3
PMMA((PhS) ₄ PcZn) (F)	21	36.4	207.9	7.5 \pm 0.3	3.0 \pm 0.1

^a In the first column (S) implies experiments in solution while (F) implies experiments in solid-state. σ_i denotes the roughness of the film—air interface, L the optical path length, α_0 the linear absorption coefficient, κ the ratio of excited to ground-state absorption cross-sections, and F_{sat} the saturation energy density. (α_0 , κ , and F_{sat} were determined at 532 nm excitation.)

fits to the data using the expressions detailed in section 2 where the spatial distribution of the energy in the pulse has been considered in all cases. The results obtained from the fitting are presented in Table 2, where all fits converged with R^2 values in excess of 0.99. It can be seen that the trend observed in solution where the (PhS)₄PcZn compound outperforms the *t*Bu₄PcZn phthalocyanine is repeated in the solid-state where the PMMA((PhS)₄PcZn) film exhibits a larger nonlinear optical response compared to the PMMA(*t*Bu₄PcZn) composite film. The nonlinear absorption coefficients exhibited by the solutions was calculated to be $\approx (2.8 \pm 0.5) \times 10^{-8}$ and $(3.9 \pm 0.6) \times 10^{-8}$ cm W⁻¹ for the *t*Bu₄PcZn and (PhS)₄PcZn compounds, respectively, whereas for the films, the nonlinear absorption coefficients were determined to be $\approx (5.7 \pm 0.9) \times 10^{-6}$ and $(6.2 \pm 1.0) \times 10^{-6}$ cm W⁻¹ for PMMA(*t*Bu₄PcZn) and PMMA((PhS)₄PcZn), respectively. It can be seen that the κ coefficient exhibited by the solid-state films is in general approximately 0.6 times that value exhibited by the corresponding solution while the F_{sat} magnitude was seen to drop by approximately a factor of 0.5 and 0.4 for the PMMA(*t*Bu₄PcZn) and PMMA((PhS)₄PcZn) composite films compared to their respective solutions.

5. Conclusions

The nonlinear absorption coefficient that was presented in section 2 is a simplified mathematical expression that can be utilized to quantify the magnitude of positive nonlinear responses in terms of two “yardstick” parameters κ and F_{sat} relating to the molecular orbital system that was discussed. The consideration of the spatial distribution of the pulses energy that was

folded with this nonlinear absorption coefficient is in general a separate issue. In fact, regardless of the form of the absorption coefficient that is used in such analysis the spatial resolution of the pulse should be considered when modeling the system. In this case, it has been shown that omission of such spatial consideration would lead to an underestimation of the calculated coefficients (κ will be understated and F_{sat} overstated), and one can reasonably assume inaccuracies would be obtained regardless of the form of the nonlinear absorption coefficient, and indeed it would be not unreasonable to assert that exploitation of such a method, despite it being computationally intensive, could benefit analysis of other systems pumped with Gaussian pulses also.

In summary, we have presented a method to assess the nonlinear absorptive response of a reverse saturable system based on two parameters that allows a quantitative determination of the optical response without the necessity for time-resolved measurements, where we have folded the spatial resolution of the incident pulses energy distribution within an algorithm that was developed for the analysis. We have demonstrated and produced high quality, relatively smooth, polymer-phthalocyanine composite films and grown them thicker using multi-layer spin casting where these composites were prepared with PMMA as the host. The optical limiting performances of these films has been tested and mathematically modeled. It can clearly be observed from Figure 6 and the corresponding numerical parameter presented in Table 2 that the solution and solid-state optical responses are very different. This was not unexpected given the nature of the change of the system while changing from solution to solid-state, and a discussion of effects due to, for example, film thickness or polymer to phthalocyanines mass ratios is reserved until a later date. It is our immediate intention to produce a large dataset from repeated measurements with structurally different phthalocyanines to identify those structures which exhibit the most efficient limiting responses in the solid-state, and potentially unravel molecular design rules linking the phthalocyanine structure to its' nonlinear optical response.

Acknowledgment. The Dublin group acknowledges financial support from Enterprise Ireland, the Irish Higher Education

Authority (HEA), and the European Union under Contract Number HPRN-CT-2000-00020.

References and Notes

- (1) Mckeown, N. B. *Phthalocyanine Materials: Synthesis, Structure and Function*; Cambridge University Press: Cambridge, U.K., 1998.
- (2) Coulter, D. R.; Miskowski, V. M.; Perry, J. W.; Wei, T. H.; Stryland, E. W. V.; Hagan, D. J. *Proc. SPIE* **1989**, 1105, 42.
- (3) de la Torre, G.; Vazquez, P.; Agullo-Lopez, F.; Torres, T. *J. Mater. Chem.* **1998**, 8, 1671.
- (4) Henari, F. Z.; Blau, W. J.; Milgrom, L. R.; Yahioğlu, G.; Phillips, D.; Lacey, J. A. *Chem. Phys. Lett.* **1997**, 267, 229.
- (5) Qu, S. L.; Chen, Y.; Wang, Y. X.; Song, Y. L.; Liu, S. T.; Zhao, X. L.; Wang, D. Y. *Mater. Lett.* **2001**, 51, 534.
- (6) Chen, Y.; O'Flaherty, S.; Fujitsuka, M.; Hanack, M.; Subramanian, L. R.; Ito, O.; Blau, W. J. *Chem. Mater.* **2002**, 14, 5163.
- (7) Auger, A.; Blau, W. J.; Burnham, P. M.; Chambrier, I.; Cook, M. J.; Isare, B.; Nekelson, F.; O'Flaherty, S. M. *J. Mater. Chem.* **2003**, 13, 1042.
- (8) Chen, Y.; Subramanian, L. R.; Fujitsuka, M.; Ito, O.; O'Flaherty, S.; Blau, W. J.; Schneider, T.; Dini, D.; Hanack, M. *Chem.-Eur. J.* **2002**, 8, 4248.
- (9) Garcia-Frutos, E. M.; O'Flaherty, S. M.; Maya, E. M.; de la Torre, G.; Blau, W.; Vazquez, P.; Torres, T. S. *J. Mater. Chem.* **2003**, 13, 749.
- (10) Shirk, J. S.; Pong, R. G. S.; Flom, S. R.; Heckmann, H.; Hanack, M. *J. Phys. Chem. A* **2000**, 104, 1438.
- (11) Mendonca, C. R.; Batista, P. S.; de Souza, M. F.; Zilio, S. C. *Chem. Phys. Lett.* **2001**, 343, 499.
- (12) Wen, T. C.; Lian, I. D. *Synth. Met.* **1996**, 83, 111.
- (13) Yamashita, M.; Inui, F.; Irokawa, K.; Morinaga, A.; Tako, T.; Mito, A.; Morawaki, H. *Appl. Surf. Sci.* **1998**, 130–132, 883.
- (14) O'Flaherty, S. M.; Hold, S. V.; Cook, M. J.; Torres, T.; Chen, Y.; Hanack, M.; Blau, W. J. *Adv. Mater.* **2003**, 15, 19.
- (15) Nitschke, C.; O'Flaherty, S. M.; Doyle, J.; Kröll, M.; Blau, W. J. *Chem. Phys. Lett.* **2004**, 383, 555.
- (16) Nitschke, C.; O'Flaherty, S. M.; Kröll, M.; Blau, W. J. *J. Phys. Chem. B* **2004**, 108, 1287.
- (17) Perry, J. W.; Mansour, K.; Lee, I. Y. S.; Wu, X. L.; Bedworth, P. V.; Chen, C. T.; Ng, D.; Marder, S. R.; Miles, P.; Wada, T.; Tian, M.; Sasabe, H. *Science* **1996**, 273, 1533.
- (18) Miles, P. *Appl. Opt.* **1999**, 38, 566.
- (19) Miles, P. A. *Appl. Opt.* **1994**, 33, 6965.
- (20) Xia, T. J.; Hagan, D. J.; Dogariu, A.; Said, A. A.; VanStryland, E. W. *Appl. Opt.* **1997**, 36, 4110.
- (21) Aneeshkumar, B.; Gopinath, P.; Vallabhan, C. P. G.; Nampoory, V. P. N.; Radhakrishnan, P.; Thomas, J. *J. Opt. Soc. Am. B* **2003**, 20, 1486.
- (22) Hercher, M. *Appl. Opt.* **1967**, 6, 947.